Inorganic Chemistry

pubs.acs.org/IC Article

Robust Aluminum and Iron Phosphinate Metal–Organic Frameworks for Efficient Removal of Bisphenol A

Daniel Bůžek, Soňa Ondrušová, Jan Hynek, Petr Kovář, Kamil Lang, Jan Rohlíček, and Jan Demel*

Cite This: https://dx.doi.org/10.1021/acs.inorgchem.0c00201 Read Online

ACCESS | Metrics & More | Article Recommendations | Supporting Information

ABSTRACT: Porous metal–organic frameworks (MOFs) have excellent characteristics for the adsorptive removal of environmental pollutants. Herein, we introduce a new series of highly stable MOFs constructed using Fe^{3+} and Al^{3+} metal ions and bisphosphinate linkers. The isoreticular design leads to ICR-2, ICR-6, and ICR-7 MOFs with a honeycomb arrangement of linear pores, surface areas up to 1360 $m^2\ g^{-1}$, and high solvothermal stabilities. In most cases, their sorption capacity is retained even after 24 h of reflux in water. The choice of the linkers allows for fine-tuning of the pore sizes and the chemical nature of the pores. This feature can be utilized for the optimization of host–guest interactions between molecules and the pore walls. Water pollution by various endocrine disrupting chemicals has been considered a global threat to public health. In this work, we prove that the chemical stability and hydrophobic nature of the synthesized series of MOFs result in the remarkable sorption properties of these materials for endocrine disruptor bisphenol A.

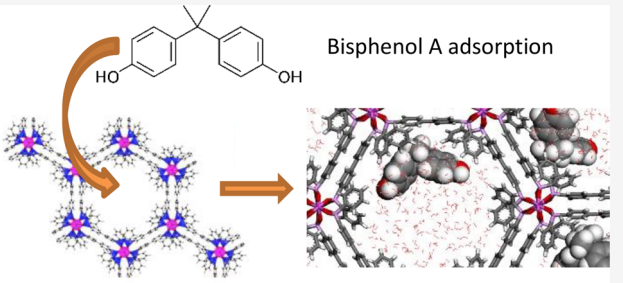

Isoreticular design of phosphinic acid-based ICR MOFs

INTRODUCTION

Endocrine disrupting chemicals are gaining increased attention among emerging pollutants due to their influence on the endocrine system, such as mimicking or blocking natural hormones and causing the over- or under production of specific hormones.[1] This diverse group of pollutants is utilized in a broad spectrum of human-made products, such as herbicides (DDT and Propanil), antimicrobial agents (Triclosan), detergents, toiletries, cosmetics (parabens and phenols), pharmaceuticals (diethylstilbestrol), and plastics (phthalates, bisphenol A, and brominated flame retardants).[1,2] The most studied endocrine disruptor is bisphenol A (2,2-bis(4-hydroxyphenyl)propane, BPA). Over a million tons of BPA are produced per year, mainly for the production of plastics such as polycarbonate and epoxy resins. It was found that BPA can leach from these products (e.g., beverage containers and packages, baby bottles, and dental sealants), migrate into the environment, and enter the food chain.[2−4] Therefore, methods for the fast and effective removal of BPA from wastewater or landfill leachate are of great importance. Commonly used sorbents, such as activated charcoal, zeolites, or clays, have a low affinity toward BPA or a low sorption capacity.[5,6] For these reasons, new materials have to be developed in order to stop the spread of endocrine disruptors in the environment.

Metal–organic frameworks (MOFs) belong to the fast growing area of organic–inorganic coordination polymers. MOFs combine metal nodes (secondary building units, SBUs) and polytopic organic ligands (linkers).[7] The number of possible SBUs and organic linkers gives rise to thousands of new structures with varying topologies, pore sizes, and chemical compositions.[8−10] The high surface area of MOFs[11,12] and the possibility to introduce functional groups[13,14] makes them highly promising materials for many applications,[15] including as sorbents of pollutants.[16−18] In this context, utilization in an aqueous environment represents a challenging condition for MOFs due to hydrolytic cleavage of the coordination bonds that constitute the MOF backbone. Thus, the number of proven water-stable MOFs is limited so far.[19] Reported water-stable MOFs are often composed of azolate linkers and M^{2+}, e.g., ZIF-8,[20] or carboxylate or phosphonate linkers combined with M^{3+} and M^{4+} metal ions as in the case of MIL-125 and UPG-1, respectively.[21,22]

Recently, we demonstrated that the combination of Fe^{3+} ions with the bisphosphinate linker H_2PBP(Me) (Figure 1) leads to a new MOF with a honeycomb structure named Fe-ICR-2 (ICR stands for Inorganic Chemistry Řež).[23] Importantly, Fe-ICR-2 is endowed with a higher hydrothermal stability in comparison to the carboxylate-based analogue Fe-MIL-53.[24] The stability is related to the stronger coordination bonds of the phosphinates to hard metals, such as Fe^{3+}, in comparison with the carboxylate groups. Notably, the methyl group bound at the phosphorus atom is pointing into the

Received: January 20, 2020

https://dx.doi.org/10.1021/acs.inorgchem.0c00201
Inorg. Chem. XXXX, XXX, XXX−XXX

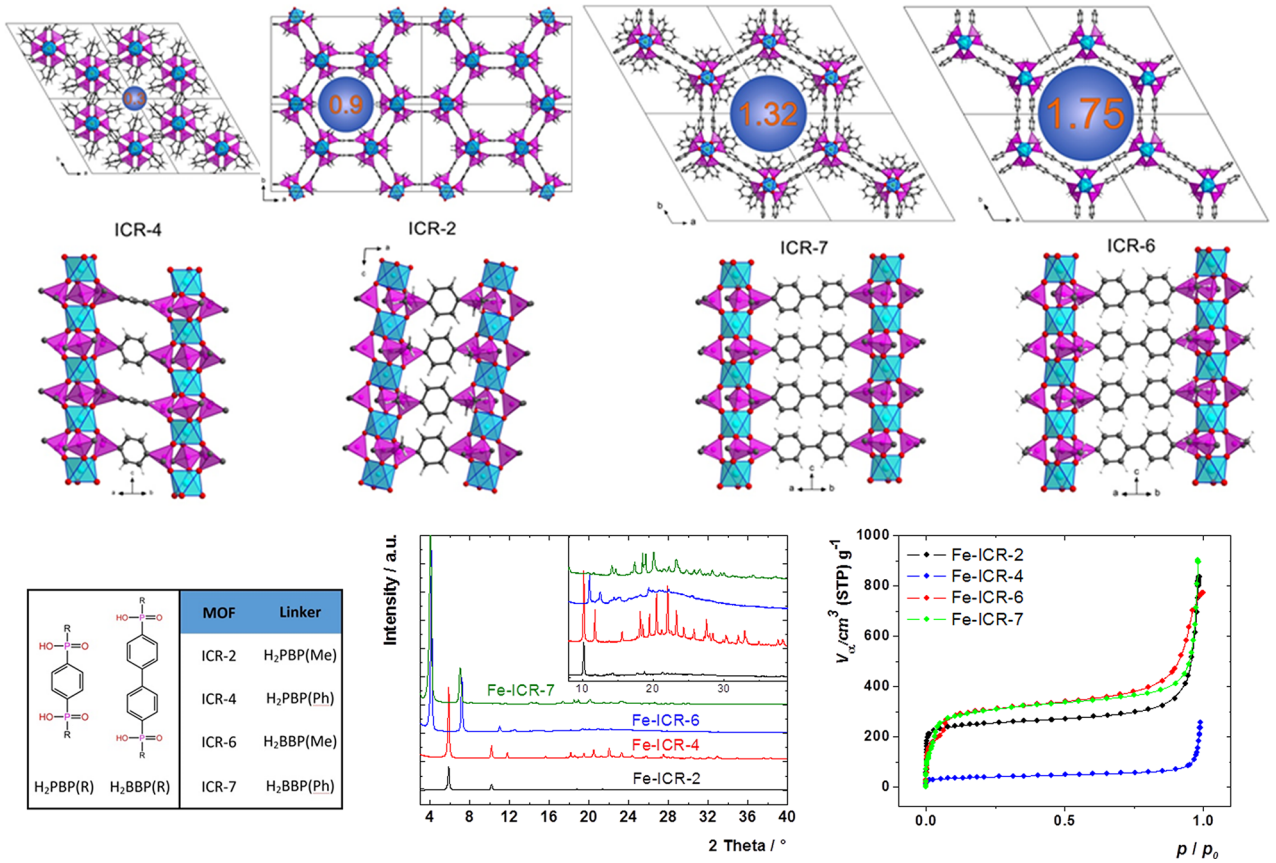

Figure 1. Honeycomb patterns of the 1D pores of the Fe-ICR MOFs running along the *c*-axis (top), where the pore limiting diameter (nm) calculated by Poreblazer is indicated in the middle of the pore; 1D columns of the octahedrally coordinated iron atoms bridged by the phosphinate acid groups (middle); coding of the ICR MOFs (bottom left); PXRD of the Fe-ICR MOFs (bottom middle); and adsorption isotherms of nitrogen for the Fe-ICR MOFs (bottom right). Color coding is as follows: octahedrally coordinated iron atoms (blue), phosphinate tetrahedra (magenta), O (red), C (gray), and H (white).

volume of the Fe-ICR-2 pore. Substitution with a bulkier phenyl group leads to a decrease in the pore size (Fe-ICR-4),[23] suggesting that this strategy can allow for fine-tuning of the pore hydrophobicity.

In this work, we applied the reticular design and extended the bisphosphinate linkers. We synthesized and delineated the properties of a series of phosphinate MOFs denoted ICR-2, ICR-4, ICR-6, and ICR-7 as both the Fe^{3+} and Al^{3+} versions (Figure 1). All prepared MOFs possess the honeycomb arrangement of linear pores, with sizes varying from 3 to 24 Å. The hydrophobic nature of the pores leads to the high sorption capacity for BPA.

RESULTS AND DISCUSSION

The solvothermal reaction of the bisphosphinate linkers (Figure 1, bottom left) with $FeCl_3 \cdot 6H_2O$ or $AlCl_3 \cdot 6H_2O$ in EtOH at 250 °C yielded the crystalline ICR MOFs. The only exception was the reaction of $H_2BBP(Me)$ with $FeCl_3 \cdot 6H_2O$, which led to the nonporous layered material Fe-ICR-5. In this case, the synthetic conditions were optimized and the porous Fe-ICR-6 was obtained in DMF at 120 °C after a three-day reaction. However, Fe-ICR-6 is of inferior crystallinity due to the lower temperature that was used compared to the other ICR MOFs (see below). The formula of all of the synthesized MOFs is $M_2(linker)_3$ (M = Fe^{3+} or Al^{3+}, linkers are specified in Figure 1), whereas the formula of the layered Fe-ICR-5 is Fe(BBP(Me)). The composition of all of the prepared MOFs was confirmed by elemental analyses and FTIR spectra (Table S1 and Figures S1−S7).

The thermal stability of the ICR MOFs in air was investigated by thermogravimetric analyses in conjunction with differential thermal analyses and mass spectroscopy (TGA/DTA/MS) (Figures S8−S14). The TGA curves indicate that all of the prepared ICR MOFs are endowed with high thermal stabilities and contain negligible amounts of solvent or water molecules inside the pores. The least stable is Al-ICR-4, which starts to decompose at 350 °C, whereas Al-ICR-7 is the most thermally stable ICR MOF with a decomposition temperature of 550 °C.

The crystal structure of Fe-ICR-7 was obtained from powder X-ray diffraction (PXRD) data (Table S2). The indexing was performed in the DICVOL06 program,[25] and the crystal structure models were found *ab initio* using the FOX software (Supporting Information).[26] The final Rietveld fit confirms the proposed structure (Table S2 and Figure S16). The low crystallinity of Fe-ICR-6 did not allow for indexing of the PXRD pattern. Nevertheless, the isoreticular design of the ICR MOFs and the solved structures for Fe-ICR-2 and Fe-ICR-4[23] enabled the creation of a structural model, followed by geometry optimizations using the PCFF force field and the Rietveld refinement in the Materials Studio software (Figure S18).[27] The PXRD patterns of all of the Fe-ICR MOFs are compared in Figure 1, bottom middle.

https://dx.doi.org/10.1021/acs.inorgchem.0c00201
Inorg. Chem. XXXX, XXX, XXX−XXX

Table 1. Specific Surface Areas, Pore Diameters, Calculated Pore Limiting Diameters, and Accessible Surface Areas for All of the Synthesized MOFs

sample	linker	specific surface area ($m^2\ g^{-1}$)	pore diameter (nm)[a]	pore volume ($cm^3\ g^{-1}$)[b]	pore limiting diameter (nm)[c]	accessible surface area ($m^2\ g^{-1}$)[d]	pore accessible volume ($cm^3\ g^{-1}$)[e]
Fe-ICR-2	H_2PBP(Me)	906[f]	0.71	0.39	0.90	850	0.48
Fe-ICR-4	H_2PBP(Ph)	165[f]	n.a.	0.044	0.29	0	n.a.
Fe-ICR-6	H_2BBP(Me)	1134[g]	2.39	1.32	1.75	1562	1.00
Fe-ICR-7	H_2BBP(Ph)	1125[g]	2.16	0.79	1.32	1097	0.64
Al-ICR-2	H_2PBP(Me)	933[f]	0.74	0.44	0.90	876	0.48
Al-ICR-4	H_2PBP(Ph)	190[f]	n.a.	0.055	0.29	0	n.a.
Al-ICR-6	H_2BBP(Me)	1362[g]	2.34	1.59	1.75	1660	1.06
Al-ICR-7	H_2BBP(Ph)	1030[g]	2.07	1.52	1.31	1088	0.63

[a]The pore diameter was obtained by the MP plot for ICR-2 and ICR-4, otherwise by the NLDFT method. [b]Total pore volume. [c]The pore limiting diameter was calculated by the Poreblazer software. [d]The accessible surface area was calculated by the Poreblazer software. [e]The accessible pore volume was calculated by the Poreblazer software. [f]The specific surface area was calculated by the *t*-plot method. [g]BET specific surface area.

Table 2. Specific Surface Areas of As-Prepared and Treated ICR MOFs[a]

		reflux			rt			activated[b]
sample	as prepared	H_2O	EtOH	toluene	H_2O	EtOH	toluene	H_2O
Fe-ICR-2	906	738	360	790	917	952	921	969
Fe-ICR-6	1134	172	1077	1081	1195	945	1174	1092
Fe-ICR-7	1125	896	1012	1061	1065	1122	1056	1077
Al-ICR-2	933	851	806	878	887	915	908	836
Al-ICR-6	1362	171	1444	1654	1087	1126	1212	747
Al-ICR-7	1030	701	1210	1076	1099	1164	1121	908

[a]Specific surface areas are in $m^2\ g^{-1}$. The *t*-plot method was used for Fe-ICR-2 and Al-ICR-2; otherwise, BET specific surface areas are given. [b]Activation from water.

Motivated by the successful syntheses of the Fe-ICR MOFs, we investigated the structural arrangements of the aluminum-based ICR MOFs (Al-ICR MOFs). In the case of Al-ICR-4, the quality of the PXRD pattern allowed for solving the crystal structure *ab initio* using the Superflip package[28] with the histogram matching option (Figure S17). Detailed analysis of the corresponding PXRD pattern confirms nearly the identical crystal structure of Al-ICR-4 compared to Fe-ICR-4[23] (Table S2). In general, the analyses of the PXRD patterns for the Al-ICR MOFs revealed that they form identical structural motifs for each linker compared to the Fe-ICR MOFs (Figure S20).

As illustrated for the Fe-ICR MOFs (Figure 1, middle),[23] the secondary building units (SBUs) of the Fe-ICR MOFs and the Al-ICR MOFs (not applicable for Fe-ICR-5, see below for details) are composed of octahedrally coordinated metal atoms bound together through O—P—O bridges that form one-dimensional (1D) infinity columns. These columns are connected via phenylene or biphenylene bridges that form the three-dimensional (3D) honeycomb framework. The Fe and Al versions of ICR-6 and ICR-7 are isoreticular structures to Fe-ICR-2, with increased pore sizes due to the incorporated biphenylene spacer. The crystal structures of Fe-ICR-4 and Al-ICR-4 are constructed similarly to the structure of Fe-ICR-2, i.e., the honeycomb arrangement is composed of 1D infinity columns tied together by O—P—O bridges. However, the phenylene groups connecting the 1D columns are not parallel to each other but instead are crossed and rotated in neighboring layers (Figure 1, left).

The crystal structure of Fe-ICR-5 was also solved from PXRD data in this work (Table S2 and Figure S15). Its structure is layered and composed of 1D infinity columns of iron atoms coordinated by O—P—O bridges (Figure S19). In this case, the oxygen atoms are coordinated to the Fe^{3+} centers in a trigonal bipyramid formation, and every two neighboring bipyramids are edge-sharing. In the chain, the pairs of edge-shared bipyramids are connected through their vertices by four phosphinate tetrahedra. The chains form bilayers that are held together only by weak nonbonding interactions. This structural arrangement is isoreticular to Fe-ICR-3.[23] A comparison of both structures is given in Figure S19. Since Fe-ICR-5 is nonporous, this material was not further investigated.

The permanent porosity of the activated ICR MOFs was probed by measuring the N_2 adsorption isotherms at 77 K (Figure 1, bottom right; Figure S43). All adsorption isotherms display a steep N_2 uptake at low P/P_0 ratios, which is typical for microporous materials. More specifically, ICR-4 contains ultramicropores, whereas the pore diameters of ICR-6 and ICR-7 are at the borderline between micropores and mesopores (Table 1 and Figures S21−S24).

In order to better understand the porous structures of the ICR MOFs, the MOFs were computationally analyzed using the Poreblazer software[29,30] for an N_2 molecule 3.314 Å in diameter (Table 1). The obtained parameters for Fe-ICR-2 and Al-ICR-2 are in agreement with the experimental values. The calculated pore limiting diameter (PLD) of Fe-ICR-4 and Al-ICR-4 is 2.9 Å; therefore, the accessible surface area cannot be calculated. Nevertheless, the pores are still accessible to N_2, as evidenced by the corresponding adsorption isotherms (Figure 1, bottom right; Figure S43). The BET specific surface areas of Fe-ICR-7 and Al-ICR-7 fit well with the calculated values, whereas in the case of Fe-ICR-6 and Al-ICR-6 the BET specific surface areas are considerably lower, probably due to a lower crystallinity or pore blocking. The PLDs of Fe-ICR-6 and Al-ICR-6 and Fe-ICR-7 and Al-ICR-7 are considerably smaller than the pore diameters obtained by the NLDFT method from adsorption isotherms. This differ-

https://dx.doi.org/10.1021/acs.inorgchem.0c00201
Inorg. Chem. XXXX, XXX, XXX−XXX

ence can be caused by the roughness of the pore walls decreasing the smallest opening of the pores or the hydrophobic nature of the pores differing significantly from the chemical nature used by the kernel in the NLDFT method.

The synthesized ICR MOFs are expected to be chemically stable under harsh conditions, as previously described for Fe-ICR-2.[23] After treatment of the ICR MOFs in water, EtOH, and toluene at rt or under reflux, the PXRD patterns of most of the ICR MOFs remained unchanged, suggesting the preservation of the crystallinity and the original structure (Figures S25–S42). Only Fe-ICR-6, Al-ICR-6, and Al-ICR-7 recrystallized or lost crystallinity in the boiling water. Generally, the longer the linker, the lower is the stability of the MOFs. For example, UiO-66, which was made of the terephthalate linker, was stable in water and under a humid atmosphere; however, both UiO-67 and UiO-68, which were made of biphenyl-4,4′-dicarboxylate and *p*-terphenyl-4,4″-dicarboxylate linkers, respectively, decomposed when exposed to humid air.[31] This behavior is not the case for the presented ICR MOFs.

We also analyzed the effects of these treatments on the specific surface area of the MOFs (Table 2 and Figures S44–S61), except for Fe-ICR-4 and Al-ICR-4. In these two cases, small molecules such as water block the pores and were not removed even during activation (150 °C, vacuum, 24 h) when keeping the PXRD pattern intact. Fe-ICR-2, Al-ICR-2, Fe-ICR-6, Fe-ICR-7, and Al-ICR-7 retained their porosity in the tested solvents at rt, in boiling toluene, and, with the exception of Fe-ICR-2, in boiling EtOH. Interestingly, Al-ICR-6 behaved differently. The specific surface area decreased after the solvent treatments at rt, while the treatments in boiling EtOH or toluene resulted in an increase in the specific surface area; this was probably due to the formation of structural defects. In general, boiling water represents one of the most challenging conditions for MOFs. In this respect, Fe-ICR-2, Al-ICR-2, and Fe-ICR-7 preserved the majority of their porosity. Clearly, both Fe-ICR-7 and Al-ICR-7 are more solvothermally stable than the corresponding ICR-6 MOFs. This behavior can be rationalized by the hydrophobicity of the phenyl groups that point into the pore accessible volume and effectively shield the coordination bonds of the linkers.[32,33]

We also investigated the stability of the ICR MOFs in regard to activation from water, i.e., under conditions where wet MOFs are dried in air without exchanging water for another solvent before drying. Some water-stable Zr-MOFs, such as PCN-222 or NU-1000, lose porosity during the activation process from water.[34] In contrast, the phosphinate ICR MOFs, except for Al-ICR-6, display low variabilities in their surface areas, indicating the exceptional stability of the porous structure. The presented experimental results confirm that the ICR family of MOFs represents robust materials that are well-suited for applications in an aqueous environment.

Adsorption of Bisphenol A. The robustness, pore size variability, and hydrophobic nature of the pores prompted us to investigate the sorption properties of ICR MOFs in regard to hydrophobic pollutants. For these experiments, we selected the Al-ICR MOFs, as the pore volume of the Al-ICRs is greater than that of the Fe analogues, and bisphenol A (BPA), a pollutant from the family of endocrine disruptors that represents a significant threat in the food chain. The adsorption properties of the Al-ICR MOFs were analyzed using high-performance liquid chromatography (HPLC). With the exception of Al-ICR-4 (PLD of 2.9 Å), all of the other Al-ICR MOFs possess pores large enough to accommodate the BPA molecules. The kinetic curves and adsorption isotherms of the Al-ICR MOFs were compared with those of conventional activated charcoal (abbreviated as AC, Sigma-Aldrich) measured under identical conditions. Prior to all measurements, the adsorbents were activated under vacuum overnight at 80 °C.

The adsorption rate is an important factor for practical application in environmental remediation. Figure 2 depicts the recorded kinetic curves. The kinetic parameters, including the correlation factors obtained by nonlinear fitting to the pseudo-second order kinetic model, are summarized in Table 3 and Table S3, and the corresponding fits are presented in Figure S62. Interestingly, the sorption equilibrium for AC, Al-ICR-2, and Al-ICR-7 was nearly completed within 15 min. By contrast, Al-ICR-6 behaved differently. The sorption kinetics indicates two consecutive processes, where a fast initial step is followed by a slow process so that the equilibrium is not reached with the time frame of the sorption experiment (i.e., 360 min). This behavior can be attributed to the slow rearrangement of BPA molecules inside the pores, indicated by

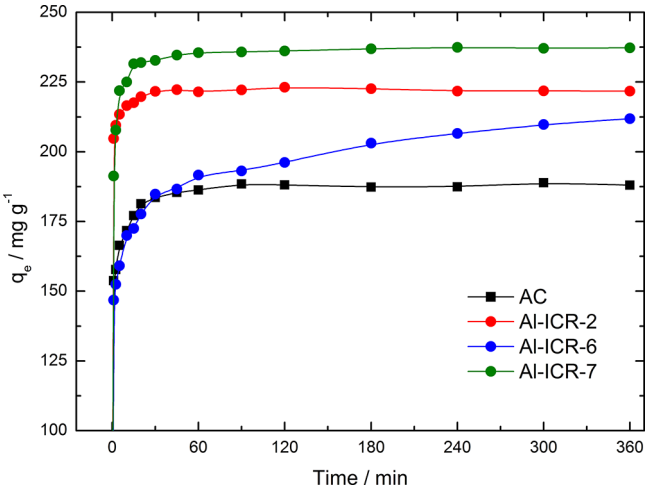

Figure 2. Kinetics of BPA adsorption by the Al-ICR MOFs compared with that of AC. Reaction conditions are as follows: an initial BPA concentration of 50 mg L^{-1} and 10 mg of the adsorbent dispersed in 50 mL of BPA solution at 25 ± 1 °C. The experimental points are obtained from triplicate experiments (see Figure S62 for error bars).

Table 3. Pseudo-Second Order Kinetic Constants and Langmuir Isotherm Constants Obtained by Nonlinear Fitting to the Experimental Data[a]

	kinetic constants		Langmuir constants	
sample	q_m (mg g^{-1})	k_2 (g mg^{-1} min^{-1})	Q_m (mg g^{-1})	K_L (L mg^{-1})
AC	183 ± 2	0.022 ± 0.001	221 ± 4	0.81 ± 0.04
Al-ICR-2	220 ± 7	0.052 ± 0.002	222 ± 3	9.61 ± 0.51
Al-ICR-4	n.a.	n.a.	22 ± 1	0.64 ± 0.58
Al-ICR-6	194 ± 4	0.010 ± 0.002	326 ± 8	0.15 ± 0.01
Al-ICR-7	234 ± 1	0.017 ± 0.002	307 ± 5	0.62 ± 0.07

[a]All data points were measured in triplicate experiments: q_m is the amount of BPA adsorbed at equilibrium, k_2 is the pseudo-second order kinetic rate constant, Q_m is the Langmuir maximum sorption capacity, and K_L is the Langmuir constant.

https://dx.doi.org/10.1021/acs.inorgchem.0c00201
Inorg. Chem. XXXX, XXX, XXX–XXX

molecular modeling. These results show that BPA can be arranged in two positions in the pores of Al-ICR-6 (for details, see below).

Adsorption isotherms of BPA for the Al-ICR MOFs and AC (Figure 3) were obtained using initial BPA concentrations

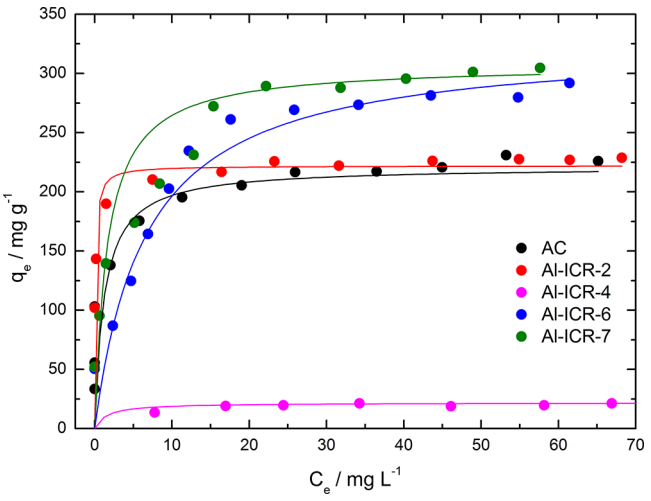

Figure 3. Adsorption isotherms of BPA expressed as the dependence of the adsorbed amount of BPA (q_e) on the BPA equilibrium concentration (C_e). The experimental points were obtained from triplicate experiments, and the solid lines are the corresponding nonlinear fits to the Langmuir adsorption model. For details, see the Supporting Information. Conditions are as follows: an initial BPA concentration between 10 and 120 mg L^{-1} and 10 mg of the adsorbent dispersed in 50 mL of BPA solution at 25 ± 1 °C.

from 10 to 120 mg L^{-1} after 24 h of stirring at a constant temperature (25 ± 1 °C). The experimental data were fitted using the Langmuir, Freundlich, and Langmuir–Freundlich adsorption isotherm models (Supporting Information). Best fits were obtained using the Langmuir model using the parameters summarized in Table 3. The results indicate that the sorption capacity for BPA increases in the order of Al-ICR-4 < AC ≈ Al-ICR-2 < Al-ICR-7 < Al-ICR-6. The highest adsorption capacity (Q_m) was found for Al-ICR-6 (326 mg g^{-1}), which is approximately 50% greater than the Q_m of AC (221 mg g^{-1}). On the other hand, the adsorption capacity of Al-ICR-2 is comparable to that of AC, and Al-ICR-4 adsorbs very little at the external surface due to it narrow pores (PLD of 2.9 Å).

Interestingly, the course of the adsorption isotherm for Al-ICR-2 is different from the isotherms of the other adsorbents. BPA was completely adsorbed from the dispersions with initial concentrations up to 30 mg L^{-1}, and Al-ICR-2 became fully saturated at the initial BPA concentration of 50 mg L^{-1}. On the other hand, Al-ICR-6, Al-ICR-7, and AC only partially removed BPA at low initial concentrations; however, due to their high pore volumes, the Q_m values are greater than that of Al-ICR-2. This observation correlates well with the values of the K_L constants of the Langmuir isotherms (Table 3), which are the measures of the adsorbent–adsorbate affinity. Thus, the high value for Al-ICR-2 (K_L = 9.61) indicates a high affinity of BPA for Al-ICR-2. In contrast, the K_L values for Al-ICR-6 and Al-ICR-7 are more than one order of magnitude lower (0.15 and 0.62, respectively), indicating that the affinity of BPA for the ICR MOFs with larger pores is significantly lower compared to that of Al-ICR-2.

The stability of the MOFs in an aqueous medium is an important issue affecting their applicability. For this reason, we also characterized the Al-ICR MOFs by PXRD and N_2 adsorption isotherms after the sorption of BPA and regeneration, done by washing with water and acetone (Figure S64 and Table S4). These characteristics are in line with the results presented above in regard to the treatment of the Al-ICR MOFs with water at rt, confirming that the Al-ICR MOFs are stable during the sorption experiments. In addition, the adsorption process is reversible, i.e., BPA can be washed out from the pores of the Al-ICR MOFs with acetone (Supporting Information).

Summing up, the Al-ICR MOFs are endowed with greater adsorption capacities than zeolites, graphene, imprinted polymers, montmorillonite, and other materials.[5] In recent years, several MOFs were successfully tested as adsorbents of BPA. The Q_m values for typical carboxylate-based MOFs (such as Fe-MIL-100 and Cr-MIL-101) do not exceed 260 mg g^{-1}.[35] Only Al-MIL-53 displays a similar maximum sorption capacity (325 mg g^{-1}) to Al-ICR-6.[36]

Molecular Modeling. We used molecular modeling in order to analyze the interactions of BPA inside the MOF pores. As described above, the pores are a hexagonal shape with the phenyl or methyl substituents bonded to P atoms aiming at the center of the pore. These substituents and the pore diameter can influence the interactions and arrangement of guest molecules as well as the sorption capacity.

The interaction energies between BPA and the Al-ICR MOFs for relevant BPA amounts adsorbed in the pores are summarized in Table 4. At low concentrations of BPA in the framework (one BPA molecule per pore in the supercell, i.e., q_e ≈ 10 mg g^{-1}), the interaction energies decrease in the order Al-ICR-2 > Al-ICR-6 > Al-ICR-7. Snapshots of the BPA arrangements are given in Figure 4a–c. The interaction energies in the Al-ICR-2 pores are nearly flat up to the loading of approximately 200 mg g^{-1}. This behavior is in good agreement with the observed high affinity of BPA for Al-ICR-2, indicated by the nearly quantitative adsorption of BPA at these concentrations and a high K_L value.

Interestingly, there are two positions for BPA in the Al-ICR-6 pore (Figure S65), with an interaction energy difference of

Table 4. Interaction Energies between BPA and Al-ICR MOFs per BPA Molecule[a]

	q_e (mg g^{-1})			
sample	10	100	200	300
Al-ICR-2	−22.2 ± 0.4	−21.3 ± 0.3	−21.2 ± 0.3	n.a.
Al-ICR-6	−20.3 ± 0.4[b]	−17.7 ± 0.2	−17.6 ± 0.2	−16.4 ± 0.2
Al-ICR-7	−18.2 ± 0.4	−16.3 ± 0.3	−16.3 ± 0.2	−15.3 ± 0.5

[a] q_e is the adsorbed amount of BPA per gram of the Al-ICR MOF. Interaction energies are given in kcal mol^{-1}. [b] The interaction energy is the weighted average over two BPA positions, as shown in Figure S65.

https://dx.doi.org/10.1021/acs.inorgchem.0c00201
Inorg. Chem. XXXX, XXX, XXX–XXX

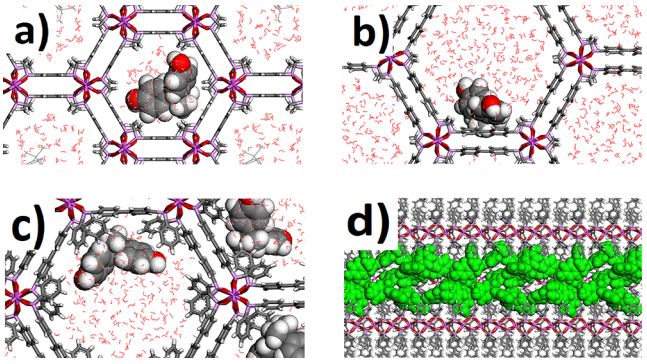

Figure 4. BPA molecules in the 1D pores of (a) Al-ICR-2, (b) ICR-6, and (c) ICR-7 with a view along the *c*-axis, $q_e \approx 10$ mg g^{-1}. (d) Arrangement of the BPA molecules in the 1D pore of Al-ICR-6 with a view perpendicular to the *c*-axis, $q_e \approx 30$ mg g^{-1}.

2.9 kcal mol^{-1} (Supporting Information). The existence of two binding sites and the relocation of the BPA molecule between these two sites during the simulation can be the reason for the measured slow adsorption kinetics (Figure 2). At higher BPA concentrations (up to $q_e \approx 300$ mg g^{-1}), the interaction energy decreases due to the BPA-BPA stacking interactions making the system quite disordered (Figure 4d and Figure S66). The average interaction energies for Al-ICR-6 and Al-ICR-7 decrease with the increasing loading of BPA, in agreement with the low K_L values found for these materials (Table 3).

CONCLUSIONS

We synthesized new ICR-6 and ICR-7 MOFs that were isoreticular with Fe-ICR-2 and Fe-ICR-4 MOFs described earlier.[23] We also showed that Al^{3+} cations can be successfully used for the construction of ICR MOFs. ICR MOFs have high thermal and solvothermal stability. Due to the hydrophobic character of the ICR pore walls, ICR MOFs effectively adsorb BPA with greater sorption capacities than the majority of already-investigated adsorbents.

Summing up, this work extends the area of phosphinic acid-based MOFs. The isoreticular design is applicable, and the wide variety of water-stable MOFs can be prepared using various substituents at the phosphorus atom. We envision that the number of phosphinic acid-based MOFs will steeply increase in the coming years.[37]

EXPERIMENTAL SECTION

Preparation of Fe-ICR-2, Fe-ICR-4, Fe-ICR-7, and Al-ICR MOFs. A Teflon lined autoclave (Berghof DAB-2) was charged with 0.08 mmol of linker and 0.04 mmol of $FeCl_3 \cdot 6H_2O$ (10.8 mg) or $AlCl_3 \cdot 6H_2O$ (9.7 mg) and overlaid with 5 mL of absolute EtOH. The sealed autoclave was heated in a preheated heating mantle (Berghof BTC-3000) at 250 °C for 24 h. The resulting white powder was centrifuged (11,000 rpm, 5 min, Hettich Rotina 380 R), washed five times with EtOH (the third time, the powder was left in EtOH for 2 h), three times with water (the second time, the powder was left in water overnight), and three times with acetone (the third time, the powder was left in acetone for 1.5 hours), and activated at 80 °C for 5 h under vacuum.

Preparation of Fe-ICR-5. A Teflon lined autoclave (Berghof DAB-2) was charged with 0.08 mmol of H_2BBP(Me) and 0.04 mmol of $FeCl_3 \cdot 6H_2O$ (10.8 mg) and overlaid with 5 mL of absolute EtOH. The sealed autoclave was heated in a preheated heating mantle (Berghof BTC-3000) at 250 °C for 24 h. The resulting white powder was centrifuged (11,000 rpm, 5 min, Hettich Rotina 380 R), washed five times with acetone, and dried in air.

Preparation of Fe-ICR-6. A Wheaton vial was charged with 37.2 mg of H_2BBP(Me) (0.12 mmol) and overlaid with 25 mL of dimethylformamide (DMF). After 10 min of sonication, 16.2 mg of $FeCl_3 \cdot 6H_2O$ (0.06 mmmol) in 5 mL of DMF was added. The vial was heated in a preheated oven (Memmert UF30 plus) at 120 °C for 72 h. The resulting white powder was centrifuged (11,000 rpm, 5 min, Hettich Rotina 380 R) and washed as described for Fe-ICR-2.

Stability of the ICR MOFs. Twenty milligrams of the MOF was suspended in 10 mL of H_2O, EtOH, or toluene, and the suspension was shaken for 24 h at rt or refluxed for 24 h. After that, the solid material was collected by centrifugation and washed twice with water (only in the case of the stability tests in water) or EtOH (only in the case of stability tests in EtOH and toluene) and twice with acetone. The resulting powders were air dried at rt.

Adsorption of BPA. The adsorption experiments were performed in sealed 100 mL reagent SIMAX glass bottles in a temperature-controlled room with a constant temperature of 25 ± 1 °C and BPA concentrations between 10 and 120 mg L^{-1}. The bottles were charged with 10 mg of the Al-ICR MOF or activated charcoal (AC, DARCO, 100 mesh particle size, powder, Sigma-Aldrich) and 10 mL of water, followed by 5 min of sonication. Then, 40 mL of a BPA solution was added. The mixture was stirred for 24 h at 25 °C, and then 1 mL of sample was taken and filtered through a PTFE microfilter (0.2 μm, Whatman). The remaining concentration of BPA was analyzed using HPLC-DAD.

ASSOCIATED CONTENT

Supporting Information

The Supporting Information is available free of charge at https://pubs.acs.org/doi/10.1021/acs.inorgchem.0c00201.

Detailed experimental procedures, FTIR spectra, PXRD patterns, Rietveld fits, TGA curves, details for the adsorption of BPA, and details of the molecular modeling (PDF)

General ICR MOF crystal structure (XYZ)

Accession Codes

CCDC 1919607−1919608 and 1980135 contain the supplementary crystallographic data for this paper. These data can be obtained free of charge via www.ccdc.cam.ac.uk/data_request/cif, or by emailing data_request@ccdc.cam.ac.uk, or by contacting The Cambridge Crystallographic Data Centre, 12 Union Road, Cambridge CB2 1EZ, UK; fax: +44 1223 336033.

AUTHOR INFORMATION

Corresponding Author

Jan Demel − *Institute of Inorganic Chemistry of the Czech Academy of Sciences, 250 68 Husinec-Řež, Czech Republic;* orcid.org/0000-0001-7796-6338; Email: demel@iic.cas.cz

Authors

Daniel Bůžek − *Institute of Inorganic Chemistry of the Czech Academy of Sciences, 250 68 Husinec-Řež, Czech Republic; Faculty of Environment, Jan Evangelista Purkyně University, 400 96, Czech Republic;* orcid.org/0000-0002-7387-9461

Soňa Ondrušová − *Institute of Inorganic Chemistry of the Czech Academy of Sciences, 250 68 Husinec-Řež, Czech Republic*

Jan Hynek − *Institute of Inorganic Chemistry of the Czech Academy of Sciences, 250 68 Husinec-Řež, Czech Republic;* orcid.org/0000-0003-1883-9464

Petr Kovář − *Charles University, Faculty of Mathematics and Physics, 121 16 Praha 2, Czech Republic*

Kamil Lang − *Institute of Inorganic Chemistry of the Czech Academy of Sciences, 250 68 Husinec-Řež, Czech Republic;* orcid.org/0000-0002-4151-8805

https://dx.doi.org/10.1021/acs.inorgchem.0c00201
Inorg. Chem. XXXX, XXX, XXX−XXX

Jan Rohlíček − *Institute of Physics of the Czech Academy of Sciences, 182 21 Praha, Czech Republic;* orcid.org/0000-0001-6913-2667

Complete contact information is available at: https://pubs.acs.org/10.1021/acs.inorgchem.0c00201

Notes

The authors declare no competing financial interest.

■ ACKNOWLEDGMENTS

This work was supported by the Czech Science Foundation (no. 20-04408S) and partial project DPK/2018/14 from the Technology Agency of the Czech Republic (GAMA COMNID TG02010049). X-ray diffractometers were supported by the Operational Program Research, Development, and Education financed by the European Structural and Investment Funds and the Ministry of Education, Youth, and Sports (no. SOLID21 CZ.02.1.01/0.0/0.0/16_019/0000760). Computational resources were supplied by the project "e-Infrastruktura CZ" (e-INFRA LM2018140) provided within the program Projects of Large Research, Development, and Innovations Infrastructures. The authors acknowledge the assistance provided by the Research Infrastructure NanoEnviCz, supported by the Ministry of Education, Youth, and Sports of the Czech Republic under Project no. LM2018124.

■ REFERENCES

(1) Nowak, K.; Jabłońska, E.; Ratajczak-Wrona, W. Immunomodulatory Effects of Synthetic Endocrine Disrupting Chemicals on the Development and Functions of Human Immune Cells. *Environ. Int.* **2019**, *125*, 350−364.

(2) Galloway, T. S.; Lee, B. P.; Burić, I.; Steele, A. M.; BPA Schools Study Consortium; Kocur, A. L.; Pandeth, A. G.; Harries, L. W. Plastics Additives and Human Health: A Case Study of Bisphenol A (BPA). In *Plastics and the Environment*; Hester, R. E., Harrison, R. M., Eds.; Royal Society of Chemistry: Cambridge, U.K., 2019; pp 131−155.

(3) Michałowicz, J. Bisphenol A − Source, toxicity and biotranformation. *Environ. Toxicol. Pharmacol.* **2014**, *37*, 738−758.

(4) Nam, S. H.; Seo, Y. M.; Kim, M. G. Bisphenol A Migration From Polycarbonate Babe Bottle with Repeated Use. *Chemosphere* **2010**, *79*, 949−952.

(5) Bhatnagar, A.; Anastopoulos, I. Adsorptive Removal of Bisphenol A (BPA) from Aqueous Solution: A Review. *Chemosphere* **2017**, *168*, 885−902.

(6) Wang, F.; Lu, X.; Peng, W.; Deng, Y.; Zhang, T.; Hu, Y.; Li, X. Y. Sorption Behavior of Bisphenol A and Triclosan by Graphene: Comparison with Activated Carbon. *ACS Omega* **2017**, *2*, 5378−5384.

(7) Eddaoudi, M.; Kim, J.; Rosi, N.; Vodak, D.; Wachter, J.; O'Keeffe, M.; Yaghi, O. M. Systematic Design of Pore Size and Functionality in Isoreticular MOFs and their Application in Methane Storage. *Science* **2002**, *295*, 469−472.

(8) Guillerm, V.; Kim, D.; Eubank, J. F.; Luebke, R.; Liu, X.; Adil, K.; Lah, M. S.; Eddaoudi, M. A Supermolecular Building Approach for the Design and Construction of Metal-Organic Frameworks. *Chem. Soc. Rev.* **2014**, *43*, 6141−6172.

(9) Furukawa, H.; Cordova, K. E.; O'Keeffe, M.; Yaghi, O. M. The Chemistry and Applications of Metal-Organic Frameworks. *Science* **2013**, *341*, 1230444.

(10) Kim, D.; Liu, X.; Lah, M. S. Topology Analysis of Metal-Organic Frameworks Based on Metal-Organic Polyhedra as Secondary or Tertiary Building Units. *Inorg. Chem. Front.* **2015**, *2*, 336−360.

(11) Koh, K.; Wong-Foy, A. G.; Matzger, A. J. A Porous Coordination Copolymer with over 5000 m^2/g BET Surface Area. *J. Am. Chem. Soc.* **2009**, *131*, 4184−4185.

(12) Farha, O. K.; Eryazici, I.; Jeong, N. C.; Hauser, B. G.; Wilmer, C. E.; Sarjeant, A. A.; Snurr, R. Q.; Nguyen, S. T.; Yazaydın, A. O.; Hupp, J. T. Metal-Organic Framework Materials with Ultrahigh Surface Areas: Is the Sky the Limit? *J. Am. Chem. Soc.* **2012**, *134*, 15016−15021.

(13) Ali Akbar Razavi, S.; Morsali, A. Linker Functionalized Metal-Organic Frameworks. *Coord. Chem. Rev.* **2019**, *399*, 213023.

(14) Cohen, S. M. Postsynthetic Methods for the Functionalization of Metal-Organic Frameworks. *Chem. Rev.* **2012**, *112*, 970−1000.

(15) Pettinari, C.; Marchetti, F.; Mosca, N.; Tosi, G.; Drozdov, A. Application of Metal-Organic Frameworks. *Polym. Int.* **2017**, *66*, 731−744.

(16) Drout, R. J.; Robison, L.; Chen, Z.; Islamoglu, T.; Farha, O. K. Zirconium Metal-Organic Frameworks for Organic Pollutant Adsoprtion. *Trends in Chem.* **2019**, *1*, 304−317.

(17) Bobbitt, N. S.; Mendonca, M. L.; Howarth, A. J.; Islamoglu, T.; Hupp, J. T.; Farha, O. K.; Snurr, R. Q. Metal-Organic Frameworks for the Removal of Toxic Industrial Chemicals and Chemical Warfare Agents. *Chem. Soc. Rev.* **2017**, *46*, 3357−3385.

(18) Feng, M.; Zhang, P.; Zhou, H.-C.; Sharma, V. K. Water-Stable Metal-Organic Frameworks for Aqueous Removal of Heavy Metals and Radionuclides: A Review. *Chemosphere* **2018**, *209*, 783−800.

(19) Bůžek, D.; Demel, J.; Lang, K. Zirconium Metal-Organic Framework UiO-66: Stability in an Aqueous Environment and Its Relevance for Organophosphate Degradation. *Inorg. Chem.* **2018**, *57*, 14290−14297.

(20) Luzuriaga, M. A.; Benjamin, C. E.; Gaertner, M. W.; Lee, H.; Herbert, F. C.; Mallick, S.; Gassensmith, J. J. ZIF-8 degrades in cell media, serum, and some—but not all—common laboratory buffers. *Supramol. Chem.* **2019**, *31*, 485−490.

(21) Dan-Hardi, M.; Serre, C.; Frot, T.; Rozes, L.; Maurin, G.; Sanchez, C.; Férey, G. A new photoactive crystalline highly porous titanium(IV) dicarboxylate. *J. Am. Chem. Soc.* **2009**, *131*, 10857−10859.

(22) Taddei, M.; Costantino, F.; Marmottini, F.; Comotti, A.; Sozzani, P.; Vivani, R. The first route to highly stable crystalline microporous zirconium phosphonate metal−organic frameworks. *Chem. Commun.* **2014**, *50*, 14831−14834.

(23) Hynek, J.; Brázda, P.; Rohlíček, J.; Londesborough, M. G. S.; Demel, J. Phosphinic Acid Based Linkers: Building Blocks in Metal−Organic Framework Chemistry. *Angew. Chem., Int. Ed.* **2018**, *57*, 5016−5019.

(24) Serre, C.; Millange, F.; Thouvenot, C.; Noguès, M.; Marsolier, G.; Louër, D.; Férey, G. Very Large Breathing Effect in the First Nanoporous Chromium(III)-Based Solids: MIL-53 or $Cr^{III}(OH)\cdot\{O_2C\text{-}C_6H_4\text{-}CO_2\}\cdot\{HO_2C\text{-}C_6H_4\text{-}CO_2H\}_x\cdot H_2O_y$. *J. Am. Chem. Soc.* **2002**, *124*, 13519−13526.

(25) Boultif, A.; Louer, D. Powder pattern indexing with the dichotomy method. *J. Appl. Cryst.* **2004**, *37*, 724−731.

(26) Černý, R.; Favre-Nicolin, V.; Rohlíček, J.; Hušák, M. FOX, Current State and Possibilities. *Crystals* **2017**, *7*, 1−10.

(27) *Materials Studio Modeling Environment, Release 4.3 Documentation*; Accelrys Software Inc.: San Diego, CA, 2003.

(28) Palatinus, L.; Chapuis, G. Superflip - a Computer Program for the Solution of Crystal Structures by Charge Flipping in Arbitrary Dimensions. *J. Appl. Crystallogr.* **2007**, *40*, 786−790.

(29) Sarkisov, L.; Harrison, A. Computational Structure Characterisation Tools in Application to Ordered and Disordered Porous Materials. *Mol. Simul.* **2011**, *37*, 1248−1257.

(30) Sarkisov, L.; Harrison, A. Computational structure characterisation tools in application to ordered and disordered porous materials. *Molecular Simulation* **2011**, *37* (15), 1248−1257.

(31) Lawrence, M. C.; Schneider, C.; Katz, M. J. Determining the Structural Stability of UiO-67 with Respect to Time: a Solid-State NMR Investigation. *Chem. Commun.* **2016**, *52*, 4971−4974.

(32) Bosch, M.; Zhang, M.; Zhou, H.-C. Increasing the Stability of Metal-Organic Frameworks. *Adv. Chem.* **2014**, *2014*, 182327.
(33) Burtch, N. C.; Jasuja, H.; Walton, K. S. Water Stability and Adsorption in Metal-Organic Frameworks. *Chem. Rev.* **2014**, *114*, 10575−10612.
(34) Mondloch, J. E.; Katz, M. J.; Planas, N.; Semrouni, D.; Gagliardi, L.; Hupp, J. T.; Farha, O. K. Are Zr_6-based MOFs Water Stable? Linker Hydrolysis vs. Capillary-Force-Driven Channel Collapse. *Chem. Commun.* **2014**, *50*, 8944−8946.
(35) Qin, F.-X.; Jia, S.-Y.; Liu, Y.; Li, H.-Y.; Wu, S.-H. Adsorption Removal of Bisphenol A from Aqueous Solution Using Metal-Organic Frameworks. *Desalin. Water Treat.* **2015**, *54*, 93−102.
(36) Zhou, M.; Wu, Y.-N.; Qiao, J.; Zhang, J.; McDonald, A.; Li, G.; Li, F. The Removal of Bisphenol A from Aqueous Solution by MIL-53(Al) and Mesostructured MIL-53(Al). *J. Colloid Interface Sci.* **2013**, *405*, 157−163.
(37) Nakatsuka, S.; Watanabe, Y.; Kamakura, Y.; Horike, S.; Tanaka, D.; Hatakeyama, T. Solvent-Vapor-Induced Reversible Single-Crystal-to-Single-Crystal Transformation of a Triphosphaazatriangulene-Based Metal−Organic Framework. *Angew. Chem., Int. Ed.* **2020**, *59*, 1435.

https://dx.doi.org/10.1021/acs.inorgchem.0c00201
Inorg. Chem. XXXX, XXX, XXX−XXX